Void Fraction of Air-Water Two-Phase Flows in a Vertically Placed Horizontal U-Bend

Hayashi, Kosuke
Yasui, Shosuke
Kurimoto, Ryo
Tomiyama, Akio

Void fraction of air-water two-phase flows in a vertically-placed horizontal U-bend

Kosuke Hayashi[a*], Shosuke Yasui[a], Ryo Kurimoto[a], Akio Tomiyama[a]

[a]Graduate School of Engineering, Kobe University, 1-1 Rokkodai, Nada, Kobe, Japan

Abstract

Experiments on air-water two-phase flows in a horizontal U-bend placed in the vertical plane were carried out to investigate effects of pipe bending on the void fraction. The inner diameter and the bend radius of curvature were 8 and 24.3 mm, respectively, so that the dimensionless bend diameter was 6. The flow patterns dealt with were plug, slug and annular flows. The void fractions in the bend and the straight section were measured by using quick-closing valves and the void fraction distribution was evaluated with an image processing method. The applicability of available correlations for the void fraction in the straight pipe was also discussed. For the straight pipe, the void fractions of the plug and slug flows can be accurately evaluated using the Smith correlation, whereas in the annular flow regime the Cioncolini and Thome correlation and the Mauro et al. liquid film thickness model give better agreement with the data. The bend void fractions in the downward and upward flows agree well with those for the pipe diameter of 26 mm given in literature, implying that the diameter effect on the void fraction is weak. The Usui et al. void fraction correlation gives reasonable evaluation for downward flows.

[*] Address correspondence to Dr. Kosuke Hayashi, Graduate School of Engineering, Kobe University, 1-1 Rokkodai, Nada, Kobe, Japan. E-mail: hayashi@mech.kobe-u.ac.jp

Introduction

Piping systems with U-bends (180^o return bends) [1, 2] are utilized in various practical applications such as heat exchangers, and two-phase flows are often formed in such engineering devices. Understanding the flow pattern [3], the pressure drop [4 - 7] and the void fraction [8 - 10] in the two-phase systems is of great importance in safety operation and rational design of the devices, and therefore, many studies have been carried out so far. Correlations of the frictional pressure drop in U-bends placed in the horizontal plane have been developed in the literature and reasonable evaluation can be obtained by using them [11, 12]. On the other hand, experimental data and correlations of the void fraction in horizontal bends placed in the vertical plane, which are required to evaluate the static pressure loss in the bend, are still insufficient.

De Oliveira and Barbosa [10] measured void fractions of air-water two-phase flows at the inlet and outlet of U-bends by using an electrical capacitance method. The pipe diameter, D, was 26 mm and the dimensionless bend radius of curvature, D_B^* (= $2R_B/D$), ranged from 6.1 to 12.2, where R_B is the bend radius of curvature. The bend was placed in the vertical plane and the void fractions in the upward and downward flows were obtained. The void fraction in the bend was evaluated as the mean of the inlet and outlet values. They reported that the Chexal et al. [13] correlation for straight pipes gave better agreement with their data than the Smith [14] and Premoli et al. [15] correlations, though the agreement with the data was not sufficient. The deviation from the data could be caused by neglecting the effects of bending. Usui et al. [9] pointed out that for upward flows the bend void fraction is similar to that in a straight pipe. On the other hand, in downward flows, the bend void fraction is larger in the bend than in the straight pipe, especially when the centrifugal force in the bend is weak compared with the gravitational force. Their experiments were carried out for D = 16 mm with R_B = 90, 132.5 and 180 mm and D = 24 mm with R_B = 135 mm. Hence, $5.6 \leq D_B^* \leq 11.25$. Although Usui et al. [9] developed a correlation for the bend void fraction in downward flows, which

is expressed in terms of the void fraction in the straight pipe and the bend Froude number, the correlation has not been sufficiently assessed yet mainly due to the lack of experimental data, especially for small D used in practical application, e.g. air-conditioning systems.

In this study, the characteristics of the void fraction of air-water two-phase flows in a U-bend of D smaller than in the literature were investigated, i.e. D = 8 mm, R_B = 24.3 mm and D_B^* = 6. In the following section, the void fraction in the straight pipe, which is required to evaluate the influence of the bend and to use the Usui et al. [9] correlation, is first discussed. The bend effect on the void fraction is then discussed using high-speed video images. For this purpose, the time-strip image analysis proposed by Borhani et al. [16] is used. The bend void fractions of downward and upward flows are shown and the applicability of the available void fraction correlations is examined for the present data.

Experimental

Figure 1 shows the experimental setup. Water and air supplied by the pump (Iwaki, MD-70R) and the compressor (Anest Iwata, SLP-110), respectively, flowed into the mixing section. A two-phase flow was then formed in the hydraulic entrance section of 1,000 mm long. The test section consisted of the straight pipe of 1,066 mm and the U-bend. The two-phase flow entered the downstream straight pipe and was discharged to the reservoir tank and atmosphere. The liquid flowmeters (Nippon Flow Cell, SCO-4, FTL) and the gas flowmeters (Nippon Flow Cell, C8960, D7954, NSPO-4) were used for measuring the volume flow rates of the two phases. The liquid and gas flow meters were calibrated using a capturing method and a water replacement method, respectively. The measurement error in the gas flow rate was confirmed to be less than 5%. The liquid volume flow rate measured by the liquid flowmeter was corrected by directly collecting water

discharged from the piping in each experimental run. The experiments were carried out at room temperature of 25±0.5ºC and atmospheric pressure.

The measurement of the volume-averaged void fraction, α, was carried out for the bend of D = 8 mm and R_B = 24.3 mm. The bend was made of two acrylic blocks to assure the circular cross section and the constant bend radius of curvature (see [11] for the detail). Figure 2 shows the bend configuration. The quick-closing valves were mounted at the inlet and outlet of the bend. The configuration of the quick-closing valve was similar to that in [17]. The distance from the bend edge to the valve was 35 mm. The length of the curved section was 75 mm. The total length of the measurement section was thus 145 mm. The third quick-closing valve was mounted 1,066 mm upstream from the quick-closing valve at the bend inlet for bypassing the fluids to the reservoir tank when the bend-side valves were closed.

The ranges of the gas and liquid volume fluxes were $0.24 \leq J_G \leq 19.7$ m/s and $0.035 \leq J_L \leq 1.41$ m/s, respectively. For flow pattern identification, two-phase flows in the bend were observed using a high-speed video camera (IDT, MotionPro X-3, 1000 fps, exposure time 350 μs) and two LED light sources for back illumination. The plug, slug and annular flows were formed in the present experimental range. The transition line between the slug and annular flows in the straight pipes agreed well with the flow pattern map developed by Barnea et al. [18], whereas for the transition between the plug and slug flows the Mandhane et al. [19] transition line fitted with the present data rather than the Barnea et al. [18] transition line.

After closing the valves, the amount of water trapped inside the bend was measured. Depending on the volume fraction, the trapped water formed either a puddle-like shape in the bottom straight section, a liquid column in the bend part or an entire liquid column with a bubble in the upper straight

section. Calibration curves converting the dimensions of the shape of the trapped water to α were prepared by injecting a prescribed amount of water into the bend.

Figure 3 shows examples of α of slug and annular flows in the bend. In the latter, the fluctuation of α is small and the mean value represented by the thick solid line converges with a small number of samples. On the other hand, the slug flow consisting of long bubbles followed by liquid slugs containing small bubbles gives large fluctuations in the data, and the number of samples required for obtaining the converged value is larger than the annular flow case. As shown by the dotted lines in the figure, the uncertainties in the mean α at 95% confidence are smaller than 5% by using the samples of 70 and 20 for the slug flow and the annular flow, respectively. The measurements were therefore repeated 70 times for plug and slug flows and 20 times for annular flow to obtain accurate values. In the measurements of α in the straight section, we could obtain well converged values of α with 20 times measurements for the three flow patterns.

Time-strip images were obtained at three positions in the bend, i.e. θ_B = π/4, π/2, 3π/4, where θ_B is the angle measured from the bottom bend edge. The flow images were taken by the high-speed video camera (1000 fps, 80 μs). For downward flows, time-strip images in the straight section were also obtained at 15 mm apart from the bend inlet. These measurement sections are shown by the broken lines in Fig. 2.

Figure 4(a) shows an example of the time-strip images. The time increases from the left to the right of the image, in which the top and bottom boundaries correspond to the outer bend wall and the inner bend wall, respectively, and y is the distance from the outer bend wall (Fig. 2). The spatial resolution in the image was 0.054 mm/pix, so that 148 pixels were present for the pipe diameter. The image was binarized as shown in Fig. 4(b). The local-instantaneous void fraction, $\alpha(t, y)$ (= 0 or 1), was obtained at each time t and y and the time-averaged void fraction, $\overline{\alpha(y)}$, was evaluated as

$$\overline{\alpha(y)} = \frac{1}{T}\sum \alpha(t,y)\Delta t \tag{1}$$

where T is the sampling time and Δt (= 0.001 s) is the time duration between two sequential images. Time-strip images for time duration of 12 sec (12,000 successive images) were made and the uncertainty in the time-averaged void fraction at 95% confidence was less than 1%.

Void fraction in straight section

The void fractions in the straight section are shown in Fig. 5. The increase in the quality, x, changes the flow pattern from plug to slug to annular flow and increases α almost monotonically, where

$$x = \frac{\rho_G J_G}{\rho_G J_G + \rho_L J_L} \tag{2}$$

and ρ_G and ρ_L are the gas and liquid densities, respectively. Even with $x \sim 0.3$ in the annular flow, α are still less than 0.9.

Smith [14] proposed the following void fraction correlation by assuming the same velocity head for the annular liquid film and the homogeneous mixture of the gas core and droplets in it:

$$\alpha = \left[1 + \frac{\rho_G}{\rho_L} e \left(\frac{1}{x} - 1\right) + \frac{\rho_G}{\rho_L}(1-e)\left(\frac{1}{x} - 1\right) V^*\right]^{-1} \tag{3}$$

where e is the ratio of the mass of liquid flowing in the homogeneous mixture to the total mass of liquid flowing, and V^* is the ratio of the mixture velocity to the liquid velocity given by

$$V^* = \left[\frac{\frac{\rho_L}{\rho_G} + e\left(\frac{1}{x} - 1\right)}{1 + e\left(\frac{1}{x} - 1\right)}\right]^{1/2} \tag{4}$$

Though this correlation was developed for annular flows, the correlation is known to be applicable to a wider range of experimental conditions. Smith [14] recommended $e = 0.4$ for all the flow patterns. Figure 5 shows a comparison between the measured α and the Smith [14] correlation. The correlation with $e = 0.4$ (the solid line) agrees with the data of the plug and slug flows, while the deviation from the data increases with increasing x in the annular flow regime. This implies that the entrained liquid flux is much smaller than that for $e = 0.4$. Cioncolini and Thome [20] and Thome and Cioncolini [21] developed the following e correlation for horizontal annular flows:

$$e = [1 + 279.6We_C^{-0.8395}]^{-2.209} \text{ for } 10^1 < We_C < 10^5 \tag{5}$$

where We_C is the core flow Weber number defined by

$$We_C = \frac{\rho_C J_G^2 D}{\sigma} \tag{6}$$

Here, σ is the surface tension, and the core flow density, ρ_C, is given by

$$\rho_C = \frac{x + e(1-x)}{\rho_G^{-1}x + \rho_L^{-1}e(1-x)} \tag{7}$$

Equation (5) gives $e < 0.005$ for the present annular flow conditions and the predicted values are much smaller than $e = 0.4$ as expected.

Cioncolini and Thome [22] proposed the following void fraction correlation for annular flows:

$$\alpha = \frac{hx^n}{1 + (h-1)x^n} \tag{8}$$

where h and n are functions of the gas and liquid densities given by

$$h = -2.129 + 3.129\left(\frac{\rho_G}{\rho_L}\right)^{-0.2186} \tag{9}$$

$$n = 0.3487 + 0.6513\left(\frac{\rho_G}{\rho_L}\right)^{0.5150} \tag{10}$$

The applicable range of this correlation is as follows: $0 < x < 1$, $10^{-3} < \rho_G/\rho_L < 1$, $0.7 < \alpha < 1$. The correlation is better than the Smith [14] correlation as shown in the figure (the dotted line).

Mauro et al. [23] developed a prediction model for the liquid film thickness, t_F, in horizontal annular flows (see Appendix A). Figure 6(a) shows an example of the predicted gas-liquid interface of liquid film for $J_G = 11.8$ m/s, $J_L = 0.098$ m/s and $D = 8$ mm. The liquid-film volume fraction, α_F, was evaluated from the predicted t_F. The liquid volume fraction, α_L, is given by

$$\alpha_L = \alpha_F + \alpha_e \tag{11}$$

Here α_e is the entrained-liquid volume fraction and is evaluated as

$$\alpha_e \frac{1-\alpha}{\alpha} = e \frac{1-x}{x} \frac{\rho_G}{\rho_L} \tag{12}$$

where the droplet velocity is assumed to be the same as that of the gas core. The void fraction is thus calculated as $\alpha = 1 - \alpha_L$. The predicted α shows reasonable agreement with the data at large α (Fig. 6(b)) although some (three data points out of 15) are out of the $\pm$10% error range. The calculated values are also shown in Fig. 5.

The drift-flux model expresses the void fraction as [24]

$$\alpha = \frac{J_G}{C_0 J_T + V_{Gj}} \tag{13}$$

where C_0 is the distribution parameter, V_{Gj} is the drift velocity, and $J_T = J_G + J_L$. Fitting Eq. (13) to the data gives (C_0, V_{Gj}) = (1.18, –0.044 m/s), (1.36, –0.37 m/s) and (1.07, 0.92 m/s) for the plug, slug and annular flow regimes, respectively. The drift-flux model works well as shown in Fig. 7 (the closed symbols); all the data are within the $\pm$10% error range. Franca and Lahey Jr [25] carried out experiments on two-phase flows in horizontal circular pipes of 19 mm in diameter and obtained $C_0 \approx 1.0$ and $V_{Gj} = 0.16$ m/s for plug flow and $C_0 = 1.2$ and $V_{Gj} = -0.20$ m/s for slug flow. In contrast to the result of Franca and Lahey Jr, V_{Gj} is the small negative value for the plug flows in the present pipe of 8 mm. On the other hand, the negative V_{Gj} in the slug flow regime is consistent with Franca's result. They explained the cause of the negative drift velocity in the slug flow regime by the liquid displacement experienced by gas bubbles and the liquid velocity distribution in the slug [26, 27]. The

C_0 in the annular flow regime is similar to those in [25] and V_{Gj} takes the positive value, i.e. $C_0 \approx 1.0$ and $V_{Gj} = 0.2$ and 2.7 m/s for $J_L = 0.005$ and 0.27 m/s, respectively.

Chexal et al. [13] developed a void fraction correlation based on the drift-flux model. The C_0 and V_{Gj} are given as functions of the fluid properties, the flow rates of the two phases and the pipe inclination so as to make the correlation applicable to a wide range of experimental conditions. The correlations of C_0 and V_{Gj} for air-water two-phase flows in horizontal pipes are given in Appendix B. Void fractions obtained with the Chexal et al. [13] correlation are shown by the open symbols in Fig. 5. The dependence on x is well reproduced although the values are systematically smaller than the data. The data of the annular flows are in-between the Chexal et al. [13] and Cioncolini and Thome [22] correlations. Most of the data are within the $\pm$10% error range except for the plug flow data as shown by the open symbols in Fig. 7. The deviation from the data is remarkable in the plug flow regime, i.e. the error in the calculated α of the plug flow is –45% in average. Chexal et al. [13] assumed $V_{Gj} \neq 0$ and used the same correlation for vertical flows. The correlation of V_{Gj} gives large positive values, i.e. $V_{Gj} \sim 0.7$ m/s for the present plug flow conditions, which results in the underestimation of α. Thus, a modification of the V_{Gj} correlation is required to reproduce the present data for horizontal flows in the 8 mm pipe.

Flows and void fraction distributions in bend

Figure 8 shows an example of the upward flows in the bend. The flow is an annular flow in the straight section before entering the bend. The gas phase moves towards the bend inner wall and the liquid phase moves to the opposite side. The interface becomes unstable and a breakup of the gas core takes place at the position indicated by the arrow in Fig. 8(c). Tiny bubbles are generated by the breakup event. The bend flow is therefore a slug flow and the presence of the bend causes the flow

pattern transition from annular to slug flow. The transition by the bend took place in some conditions close to the slug-annular transition line in the straight pipe. This type of flow pattern transition took place also in some downward flows.

An example of the upward plug flows in the bend is shown in Fig. 9. The liquid phase tends to migrate toward the outer bend wall due to the centrifugal force, so that the liquid film on the outer-bend-wall side becomes thick in the lower half of the bend (Fig. 9(b)). In addition, the gravitational force acting on the liquid retards the upward motion in the bend (Fig. 9(c)), which would result in a decrease in the void fraction.

Figure 10 shows the time-averaged void fraction, $\overline{\alpha(y)}$, obtained by the time-strip image analysis. The flow pattern is downward annular flow at J_G = 7.8 m/s and J_L = 0.092 m/s. The flow direction is from left to right (see Fig. 2). The vertical axis represents $D - y$, and $D - y$ = 0 and 8 mm are for the inner bend wall and the outer bend wall, respectively. In the straight section (Fig. 10(a)), $\overline{\alpha(D-y)}$ takes small values near the walls, representing the presence of the liquid film. The liquid film thickness at the bottom wall is thicker than that at the top wall due to gravity as predicted in Fig. 6(a). The distribution of $\overline{\alpha(D-y)}$ is steep at the top wall, which means that the liquid film thickness does not change in time so much. On the other hand, the smoother profile on the bottom wall side is due to fluctuations in $\alpha(t, D-y)$ by interfacial waves. $\overline{\alpha(y)} \sim 1$ in the gas core region. Even after entering the bend (Fig. 10(b)), the bend effect on $\overline{\alpha(D-y)}$ is not remarkable at $\theta_B = 3\pi/4$. However, the centrifugal force causes the migration of the liquid phase from the inner bend wall to the outer bend wall side, which results in the decrease in the film thickness on the inner bend wall and the increase in the film thickness on the outer bend wall as shown in Fig. 10(c). The change in the liquid film thickness continues as shown in Fig. 10(d) and the profile of $\overline{\alpha(D-y)}$ on the outer bend wall side is much smoother than that before entering the bend.

The $\overline{\alpha(y)}$ of an upward annular flow is shown in Fig. 11, in which y = 0 and 8 mm correspond to the outer bend wall and the inner bend wall, respectively, and Fig. 11(a) is the same as in Fig. 10(a). The liquid upward motion is retarded by the gravity in the upward flow, so that the gas-liquid interface in the bend is strongly agitated compared with the downward flow. This effect makes the $\overline{\alpha(y)}$ profile smoother as shown in Fig. 11(b) and Fig. 11(c). The liquid film thickness on the outer bend wall becomes thick in Fig. 11(c). The action of gravity however induces migration of the liquid phase toward the inner bend wall for $\theta_B \geq \pi/2$, and therefore, the film thickness on the outer bend wall side decreases at $\theta_B = 3\pi/4$ (Fig. 11(d)).

Figure 12 shows $\overline{\alpha(D-y)}$ of a downward slug flow. Large bubbles tend to flow near the top wall in the straight section due to buoyancy, so that $\overline{\alpha(D-y)}$ is asymmetric as shown in Fig. 12(a). The intermittent nature of the passage of liquid slugs and large bubbles results in $\overline{\alpha(D-y)} \sim 0.8$ for $2 < D - y < 7$ mm. Large bubbles migrate toward the inner bend wall, and therefore, $\overline{\alpha(D-y)}$ becomes larger in the small ($D - y$) region. The nose of a large bubble flows along the inner bend wall, while the liquid film thickness becomes thicker on the outer bend wall side. Consequently, $\overline{\alpha(D-y)}$ shows a peak at $D - y \sim 1$ mm and the profile (the gas phase region) moves downward from Fig. 12(b) to Fig. 12(d). In the upward slug flow shown in Fig. 13, the effect of liquid flow retardation in the bend is remarkable (Fig. 13(b) and Fig. 13(c)), i.e. the liquid film becomes thick on the outer bend wall side and disturbances on the gas-liquid interfaces make the profile smooth. The characteristics of $\overline{\alpha}$ in the downward and upward plug flows were similar to those of the slug flows.

Void fraction in bend

Figure 14 shows comparisons between α in the straight section, that in the upward flow in the bend, and that in the downward flow in the bend. The α in the bend are almost the same as those in the straight section or smaller. The differences in α between the straight section and the bend are not remarkable in the plug flow regime. In the slug flow regime, α of the downward flow is comparable to those of the straight section, while in the upward flow the presence of the bend decreases α. As discussed in the previous section, in upward slug flows, the retardation of the upward liquid motion was caused in the bend due to the gravitational force. The liquid volume fraction therefore increased, in other words, α decreased. On the other hand, the influence of the presence of the bend was weaker in the downward slug flow compared with the upward flow, so that α are close to those in the straight section except for the annular flow regime. The α in the upward and downward annular flows are almost the same. Hence, the bend effect mitigates as x increases though the presence of the bend tends to decrease α.

The plus and cross symbols in the figure represent the experimental data for D = 26 mm, R_B = 79, 113 and 159 mm (D_B^* = 6.1, 8.7 and 12.2) obtained by De Oliveira and Barbosa [10], and the former and the latter are for downward and upward flows, respectively. The α in the downward flow are larger than those in the upward flow, whereas the difference becomes small as x increases. The characteristics are the same as in the present experiment, and their data agree well with the present data except for the downward flow at $x \sim 0.001$. The agreement implies that the diameter effect is not significant for $8 \leq D \leq 26$ mm. The deviation at the small x may be attributed to the difference in D; The Usui et al. [9] data for D = 16 and 24 mm also showed that α in downward flow tends to be larger compared with horizontal and upward flows at small x and this bend effect is remarkable when R_B is large.

As shown in Fig. 15, V^* given by Eq. (4) is acceptable at low x, whereas the deviation from the data increases with increasing x. A simple modification, $V_f^* = 2.5V^{*1.9}$, gives better estimation of the velocity ratio for the slug and annular flow regimes. The α evaluated using the Smith [14] correlation with V_f^* instead of V^* agrees fairly well with the bend data as shown in Fig. 14 (the dash-dotted line).

A slight reduction in α in the upward annular flow due to the bend effect was also observed by Usui et al. [8]. Their void fraction data for the straight section agreed with the Smith [14] correlation. The effects of the bend of $D_B^* = 5.6$ on α were weak, while the increase in D_B^* made α larger (smaller) at small (large) x. However, they concluded that the bend does not have a remarkable effect on the overall trend of α. Usui et al. [9] proposed the following α correlation for downward flows, in which the bend effect is taken into account in terms of the bend Froude number:

$$\alpha = \frac{\alpha_S + 0.15/Fr_c^{0.75}}{1 + 0.15/Fr_c^{0.75}} \tag{14}$$

where α_S is the void fraction in the straight section, and Fr_c is defined as

$$Fr_c = \frac{J_L^2}{\frac{\Delta\rho g R_B}{\rho_L}(1-\alpha_S)^2}\left[1 - \frac{\rho_G}{\rho_L}\left(\frac{J_G(1-\alpha_S)}{J_L\alpha_S}\right)^2\right] \tag{15}$$

Here, $\Delta\rho$ (= $\rho_L - \rho_G$) is the density difference, and g is the magnitude of the acceleration of gravity. Figure 16 shows comparisons between the void fraction in the bend and those evaluated using Eq. (14), where α_S is calculated by using the drift-flux model with C_0 and V_{Gj} obtained by fitting to the

present data. Most data are within the ±10% error range; the deviations from the measured data are −3.9% and −8.5% in average for the downward and the upward flow data, respectively. The α of the upward flow are also reasonably evaluated using the correlation though it was developed for the downward flow.

Table 1 summarizes C_0 and V_{Gj} obtained by fitting Eq. (13) to the present data. It should be noted that, in the calculation of C_0, V_{Gj} of upward plug flow was assumed to be the same as that of upward slug flow since the number of the plug flow data were insufficient. The C_0 and V_{Gj} of the downward flows are not so different from those of the straight pipe. On the other hand, V_{Gj} of the upward flows are largely different from the other two. However, the flow direction does not affect C_0 so much. Modeling effects of D and D_B^* on C_0 and V_{Gj} is a future work.

Conclusions

The bend void fractions of air-water two-phase flows in the plug, slug and annular flow regimes were obtained and the effects of the presence of the bend on the flow characteristics and the void fraction were discussed. The pipe diameter was 8 mm and the bend radius of curvature was 24.3 mm, so that the dimensionless bend diameter was 6. The void fraction in the straight pipe was also discussed. The main conclusions are as follows:

For straight pipe

(1) The Smith [14] correlation with $e = 0.4$ is the most accurate in the plug and slug flow regimes.

(2) The Mauro et al. [23] liquid film thickness model with the e correlation proposed by Cioncolini and Thome [20, 21] is recommended for annular flows of $x > 0.1$, whereas the Cioncolini and Thome [22] correlation gives better agreement for lower x.

(3) The drift-flux model works well for the present data, i.e. the calculated values are within the ±10% error range, whereas the Chexal et al. [13] correlation based on the drift-flux model requires modifications in the correlations of C_0 and V_{Gj}.

For U-bend

(4) The presence of the bend decreases the void fraction both in downward and upward flows. The void fraction of the upward slug flow is smaller than that of the downward slug flow due to the gravitational effect, whereas the differences in the void fraction are small in the annular flow regime.

(5) The present void fraction data agree with those obtained by De Oliveira and Barbosa [10] for bends of 26 mm diameter, which implies that the diameter effect is insignificant in the range of 8 to 26 mm.

(6) The Usui et al. [9] correlation for downward flows is applicable to the present downward flow conditions, provided that the void fraction in the straight pipe, which is used in the correlation, is accurately evaluated.

An experiment with a wider range of the relevant parameters, e.g. D, D_B^* and the fluid properties, should be a future work to validate the applicability of the obtained knowledge to two-phase flows in different bend configurations.

Acknowledgements

The authors would like to express their thanks to Mr. Daisuke Masuda for his assistance in the experiments.

Appendix A Mauro et al. [23] liquid film thickness model

Mauro et al. [23] proposed the following model for the liquid film thickness in a horizontal circular channel:

$$t_F(\theta) = \begin{cases} R - \dfrac{AB}{\sqrt{A^2\cos^2\theta + B^2\sin^2\theta}} & \text{for } 0 \le \theta \le \dfrac{\pi}{2} \\ R - \dfrac{AC}{\sqrt{A^2\cos^2\theta + C^2\sin^2\theta}} & \text{for } \dfrac{\pi}{2} < \theta \le \pi \end{cases} \tag{A1}$$

where A, B and C are the distance from the channel center to the gas-liquid interface in the direction to the side, top and bottom.

$$A = \frac{2(R - t_a)^2}{B + C} \tag{A2}$$

$$B = R - t_t \tag{A3}$$

$$C = R - t_b \tag{A4}$$

The t_a is the average liquid film thickness, while t_t and t_b are the thickness at the top and bottom of the channel. The t_b is given by the following correlation proposed by Cioncolini and Thome [28]:

$$\frac{t_t}{t_b} = \frac{0.0789 Fr_G^{1.90}}{1 + 0.0789 Fr_G^{1.90}} \quad \text{for } Fr_G > 1 \tag{A5}$$

$$\frac{t_a}{t_b} = \frac{0.366 Fr_G^{1.45}}{1 + 0.366 Fr_G^{1.45}} \quad \text{for } Fr_G > 1 \tag{A6}$$

where

$$Fr_G = \frac{J_G}{\sqrt{\Delta\rho g D/\rho_G}} \tag{A7}$$

The dimensionless average liquid film thickness, t^*, defined by $t^* = t_a/y^+$ is given by the following empirical correlation:

$$t^* = \max\left(\sqrt{\frac{Re_F}{2}}, 0.0165 Re_F\right) \tag{A8}$$

where y^+ (= $\mu_L/\rho_L u^+$) is the length wall scale, u^+ (= $[\tau_w/\rho_L]^{1/2}$) is the velocity wall scale, τ_w is the average wall shear stress, μ_L is the liquid density, and Re_F is the film Reynolds number given by

$$Re_F = (1-e)(1-x)\frac{GD}{\mu_L} \tag{A9}$$

Here G is the mass flux, $G = \rho_G J_G + \rho_L J_L$. The friction factor, f, correlation proposed by Cioncolini et al. [29] is used to evaluate τ_w:

$$f = \frac{2\tau_w}{\rho_C u_C^2} = \frac{0.172}{We_C^{0.372}} \tag{A10}$$

where We_C is the core flow Weber number defined by Eq. (6), and the average core velocity, u_C, is given by

$$u_C = \frac{J_G}{\alpha} \tag{A11}$$

The entrained liquid fraction is given by Eq. (5) [20]. The void fraction is evaluated by Eq. (8) [22] in the Mauro et al. [23] prediction model. In this study, α was determined by an iterative manner to satisfy $\alpha + \alpha_F + \alpha_e = 1$, where α_F is the liquid film volume fraction evaluated for the predicted film thickness distribution and α_e is the droplet volume fraction calculated from e.

Appendix B Void fraction correlation of Chexal et al. [13]

The Chexal et al. [13] correlation covers a wide range of two-phase flows, e.g. co-current upward flows, counter-current flows, horizontal flows, water-vapor flows and air-water flows. The correlation reduced to the form for air-water two-phase flows in horizontal pipes is given in the following. The distribution parameter is given by

$$C_0 = [1 + \alpha^{0.05}(1 - \alpha)^2]C_{0v} \tag{B1}$$

where

$$C_{0v} = \frac{L}{K_0 + (1 - K_0)\alpha^{r_0}} \tag{B2}$$

$$L = \min\,[1.125\alpha^{0.6}, 1] \tag{B3}$$

$$K_0 = B_1 + (1 - B_1)\left(\frac{\rho_G}{\rho_L}\right)^{1/4} \tag{B4}$$

$$r_0 = \frac{1 + 1.57\,\rho_G/\rho_L}{1 - B_1} \tag{B5}$$

$$B_1 = \min\,[0.8, A_1] \tag{B6}$$

$$A_1 = [1 + \exp\,(-Re/60000)]^{-1} \tag{B7}$$

$$Re = \max\,[Re_G, Re_L] \tag{B8}$$

$$Re_k = \frac{\rho_k J_k D}{\mu_k} \quad (k = G \text{ or } L) \tag{B9}$$

The drift velocity is given by

$$V_{Gj} = V_{Gj}^0 (1 - \alpha)^{B_1} \tag{B10}$$

where

$$V_{Gj}^0 = 1.41 \left[\frac{\sigma \Delta \rho g}{\rho_L^2}\right]^{1/4} C_2 C_3 C_4 \tag{B11}$$

$$C_2 = \begin{cases} 1 & \text{if } C_5 \geq 1 \\ [1 - \exp\,(-C_5/(1 - C_5))]^{-1} & \text{if } C_5 < 1 \end{cases} \tag{B12}$$

$$C_3 = \max\,[0.50{,}2\exp\,[-Re_L/60000]] \tag{B13}$$

$$C_4 = \begin{cases} 1 & \text{if } C_7 \geq 1 \\ [1 - \exp\,(-C_7/(1 - C_7))]^{-1} & \text{if } C_7 < 1 \end{cases} \tag{B14}$$

$$C_5 = \sqrt{\frac{150\rho_G}{\rho_L}} \tag{B15}$$

$$C_7 = \left(\frac{D_2}{D}\right) \tag{B16}$$

where D_2 = 0.09144 m.

Nomenclature

A	function of liquid film thickness defined by Eq. (A2), m
A_1	function of Reynolds number given by Eq. (B7)
B	function of liquid film thickness defined by Eq. (A3), m
B_1	function of Reynolds number given by Eq. (B6)
C	function of liquid film thickness defined by Eq. (A4), m
C_0	distribution parameter for horizontal flow
C_{0v}	distribution parameter for vertical flow
C_i	coefficients in the Chexal et al. [13] correlation (i = 2, 3, 4, 5, 7)
D	inner pipe diameter, m
D_2	reference diameter (0.09144 m), m
D_B^*	dimensionless bend radius of curvature (= $2R_B/D$)
e	entrained liquid mass fraction
Fr_G	gas Froud number
Fr_c	Froud number for centrifugal force
f	friction factor
G	mass flux, kg/(m^2 s)
g	magnitude of acceleration of gravity, m/s^2
h	functions of density ratio given by Eq. (9)
J_G	gas volume flux, m/s
J_L	liquid volume flux, m/s
J_T	total volume flux, m/s

K_0	model parameter in the Chexal et al. [13] correlation
L	fluid property index
n	functions of density ratio given by Eq. (10)
R	pipe radius, m
R_B	bend radius of curvature, m
Re	Reynolds number
Re_F	film Reynolds number
Re_G	gas Reynolds number
Re_L	liquid Reynolds number
r	radial coordinate for bend, m
r_0	model parameter in the Chexal et al. [13] correlation
T	sampling time, s
t	time, s
t^*	dimensionless average liquid film thickness, m
t_a	average liquid film thickness, m
t_b	liquid film thickness at pipe bottom wall, m
t_F	liquid film thickness, m
t_t	liquid film thickness at pipe top wall, m
u_C	gas core velocity, m/s
u^+	velocity wall scale, m/s
V^*	velocity ratio
V_f^*	modified velocity ratio
V_{Gj}	drift velocity, m/s
V_{Gj}^0	reference drift velocity, m/s

We_C	core flow Weber number
X	Cartesian coordinate in pipe cross section, m
x	quality
Y	Cartesian coordinate in pipe cross section, m
y	distance from wall, m
y^+	length wall scale, m

Greek symbols

α	void fraction
$\alpha(t, y)$	local instantaneous void fraction
α_e	entrained-liquid volume fraction
α_F	volume fraction of liquid film
α_L	liquid volume fraction
α_S	void fraction in straight pipe
$\overline{\alpha(y)}$	time-averaged void fraction
Δt	time interval between sequential images, s
$\Delta\rho$	density difference, kg/m^3
θ	azimuthal coordinate in pipe, rad
θ_B	azimuthal coordinate for bend, rad
μ_G	gas viscosity, Pa s
μ_L	liquid viscosity, Pa s
ρ_C	core flow density, kg/m^3
ρ_G	gas density, kg/m^3

ρ_L	liquid density, kg/m^3
σ	surface tension, N/m
τ_w	wall shear stress, Pa

Subscripts

a	average
B	bend
b	bottom
C	gas core
c	centrifugal force
e	droplet
F	film
f	modification for velocity ratio, *V**
G	gas
j	quantity relative to total volume flux
L	liquid
S	straight
T	total
t	top
w	wall

Superscript

+	wall scale

*	dimensionless quantity
0	reference quantity

Abbreviation

D	downward flow
S	straight pipe
U	upward flow

References

[1] C. Koushik, and K. A. Prakash, "Steady and unsteady forced convective heat transfer analysis in 180 degree bend," *Heat Transfer Eng.*, vol. 41, no. 22, pp. 1901-1920, 2020. DOI: 10.1080/01457632.2019.1675248.

[2] R. Andrzejczyk, T. Muszynski, and P. Kozak, "Experimental and computational fluid dynamics studies on straight and U-bend double tube heat exchangers with active and passive enhancement methods," *Heat Transfer Eng.*, vol. 42, no. 3-4, pp. 167-180, 2021. DOI: 10.1080/01457632.2019.1699279.

[3] R. J. Da Silva Lima, and J. R. Thome, "Two-phase flow patterns in U-bends and their contiguous straight tubes for different orientations, tube and bend diameters," *Int. J. Refrig.*, vol. 35, no. 5, pp. 1439-1454, 2012. DOI: 10.1016/j.ijrefrig.2012.02.002.

[4] R. J. Da Silva Lima, and J. R. Thome, "Two-phase flow pressure drops in U-tubes: Towards more accurate measurement methods and prediction models," *Int. J. Refrig.*, vol. 36, no. 2, pp. 492-503, 2013. DOI: 10.1016/j.ijrefrig.2012.12.005.

[5] M. Padilla, R. Revellin, and J. Bonjour, “Prediction and simulation of two-phase pressure drop in return bends,” *Int. J. Refrig.*, vol. 32, no. 7, pp. 1776-1783, 2009. DOI: 10.1016/j.ijrefrig.2009.06.006.

[6] M. Padilla, R. Revellin, P. Haberschill, and J. Bonjour, “Two-phase pressure drop in return bends: Experimental results for R-410A,” *Int. J. Refrig.*, vol. 34, no. 8, pp. 1854-1865, 2011. DOI: 10.1016/j.ijrefrig.2011.03.009.

[7] M. Padilla, R. Revellin, J. Wallet, and J. Bonjour, “Flow regime visualization and pressure drops of HFO-1234yf, R-134a and R-410A during downward two-phase flow in vertical return bends,” *Int. J. Heat Fluid Flow*, vol. 40, pp. 116-134, 2013. DOI: 10.1016/j.ijheatfluidflow.2013.01.005.

[8] K. Usui, S. Aoki, and A. Inoue, “Flow behavior and pressure drop of two-phase flow through C-shaped bend in vertical plane, (I),” *J. Nucl. Sci. Technol.*, vol. 17, no. 12, pp. 875-887, 1980. DOI: 10.3327/jnst.17.875.

[9] K. Usui, S. Aoki, and A. Inoue, “Flow behavior and pressure drop of two-phase flow through C-shaped bend in vertical plane, (II),” *J. Nucl. Sci. Technol.*, vol. 18, no. 3, pp. 179-190, 1981. DOI: 10.3327/jnst.18.179.

[10] P. M. De Oliveira, and J. R. Barbosa, “Pressure drop and gas holdup in air-water flow in 180º return bends,” *Int. J. Multiphase Flow*, vol. 61, pp. 83-93, 2014. DOI: 10.1016/j.ijmultiphaseflow.2014.01.005.

[11] K. Hayashi, J. Kazi, N. Yoshida, and A. Tomiyama, “Effects of fluid properties on pressure drops of two-phase flows in horizontal U-bends,” *Multiph. Sci. Technol.*, vol. 32, no. 4, pp. 325-340, 2020. DOI: 10.1615/MultScienTechn.2020036154.

[12] K. Hayashi, J. Kazi, N. Yoshida, and A. Tomiyama, “Pressure drops of air-water two-phase flows in horizontal U-bends,” *Int. J. Multiphase Flow*, vol. 131, 103403, 2020. DOI: 10.1016/j.ijmultiphaseflow.2020.103403.

[13] B. Chexal, G. Lellouche, J. Horowitz, and J. Healzer, “A void fraction correlation for generalized applications,” *Prog. Nucl. Energy*, vol. 27, no. 4, pp. 255-295, 1992. DOI: 10.1016/0149-1970(92)90007-P.

[14] S. L. Smith, “Void fractions in two-phase flow: a correlation based upon an equal velocity head model,” *Proc. Inst. Mech. Eng., Part I*, vol. 184, no. 36, pp. 647-664, 1969. DOI: 10.1243/PIME_PROC_1969_184_051_02.

[15] A. Premoli, D. Francesco, and A. Prina, “A dimensionless correlation for determining the density of two-phase mixtures,” *Termotecnica*, vol. 25, pp. 17-26, 1971.

[16] N. Borhani, B. Agostini, and J. R. Thome, “A novel time strip flow visualisation technique for investigation of intermittent dewetting and dryout in elongated bubble flow in a microchannel evaporator,” *Int. J. Heat Mass Transfer*, vol. 53, no. 21-22, pp. 4809-4818, 2010. DOI: 10.1016/j.ijheatmasstransfer.2010.06.011.

[17] H. Funahashi, K. Vierow Kirkland, K. Hayashi, S. Hosokawa, and A. Tomiyama, “Interfacial and wall friction factors of swirling annular flow in a vertical pipe,” *Nucl. Eng. Des.*, vol. 330, pp. 97-105, 2018. DOI: 10.1016/j.nucengdes.2018.01.043.

[18] D. Barnea, O. Shoham, Y. Taitel, and A. E. Dukler, “Flow pattern transition for gas-liquid flow in horizontal and inclined pipes,” *Int. J. Multiphase Flow*, vol. 6, no. 3, pp. 217-225, 1980. DOI: 10.1016/0301-9322(80)90012-9.

[19] J. M. Mandhane, G. A. Gregory, and K. Aziz, “A flow pattern map for gas-liquid flow in horizontal pipes,” *Int. J. Multiphase Flow*, vol. 1, no. 4, pp. 537-553, 1974. DOI: 10.1016/0301-9322(74)90006-8.

[20] A. Cioncolini, and J. R. Thome, “Entrained liquid fraction prediction in adiabatic and evaporating annular two-phase flow,” *Nucl. Eng. Des.*, vol. 243, pp. 200-213, 2012. DOI: 10.1016/j.nucengdes.2011.11.014.

[21] J. R. Thome and A. Cioncolini, “Entrained liquid fraction in annular two-phase flow,” in *Encyclopedia of Two-Phase Heat Transfer and Flow I*. vol. 3, J. R. Thome, Ed. Singapore: World Scientific, 2015, pp. 113-142. DOI: 10.1142/9789814623216_0022.

[22] A. Cioncolini, and J. R. Thome, “Void fraction prediction in annular two-phase flow,” *Int. J. Multiphase Flow*, vol. 43, pp. 72-84, 2012. DOI: 10.1016/j.ijmultiphaseflow.2012.03.003.

[23] A. W. Mauro, A. Cioncolini, J. R. Thome, and R. Mastrullo, “Asymmetric annular flow in horizontal circular macro-channels: Basic modeling of liquid film distribution and heat transfer around the tube perimeter in convective boiling,” *Int. J. Heat Mass Transfer*, vol. 77, pp. 897-905, 2014. DOI: 10.1016/j.ijheatmasstransfer.2014.06.021.

[24] N. Zuber, and J. A. Findlay, “Average volumetric concentration in two-phase flow systems,” *J. Heat Transfer*, vol. 87, no. 4, pp. 453-468, 1965. DOI: 10.1115/1.3689137.

[25] F. Franca, and R. T. Lahey Jr, “The use of drift-flux techniques for the analysis of horizontal two-phase flows,” *Int. J. Multiphase Flow*, vol. 18, no. 6, pp. 787-801, 1992. DOI: 10.1016/0301-9322(92)90059-P.

[26] O. Kvernvold, V. Vindoy, T. Sontvedt, A. Saasen, and S. Selmer-Olsen, “Velocity distribution in horizontal slug flow,” *Int. J. Multiphase Flow*, vol. 10, no. 4, pp. 441-457, 1984. DOI: 10.1016/0301-9322(84)90055-7.

[27] K. H. Bendiksen, “An experimental investigation of the motion of long bubbles in inclined tubes,” *Int. J. Multiphase Flow*, vol. 10, no. 4, pp. 467-483, 1984. DOI: 10.1016/0301-9322(84)90057-0.

[28] A. Cioncolini, and J. R. Thome, “Liquid film circumferential asymmetry prediction in horizontal annular two-phase flow,” *Int. J. Multiphase Flow*, vol. 51, pp. 44-54, 2013. DOI: 10.1016/j.ijmultiphaseflow.2012.12.003.

[29] A. Cioncolini, J. R. Thome, and C. Lombardi, “Unified macro-to-microscale method to predict two-phase frictional pressure drops of annular flows,” *Int. J. Multiphase Flow*, vol. 35, no. 12, pp. 1138-1148, 2009. DOI: 10.1016/j.ijmultiphaseflow.2009.07.005.

Table 1. The distribution parameter, C_0, and the drift velocity, V_{Gj}, obtained by fitting to the present data (D = 8 mm and R_B = 24.3 mm). *V_{Gj} of upward plug flow is assumed to be the same as that of upward slug flow since the number of plug flow data is insufficient.

	plug		slug		annular	
	C_0	V_{Gj} [m/s]	C_0	V_{Gj} [m/s]	C_0	V_{Gj} [m/s]
straight	1.18	–0.04	1.36	–0.37	1.07	0.92
downward	1.24	0.01	1.32	–0.23	1.13	1.04
upward	1.29	0.26*	1.31	0.26	0.98	3.05

List of Figure Captions

Figure 1. Experimental setup.

Figure 2. Bend configuration.

Figure 3. Measured void fractions in bend and their mean values changing with number of samples.

Figure 4. Time-strip image of plug flow. (a) time-strip image at $\theta_B = \pi/4$; (b) binarized time-strip image and waveform of void fraction, $\alpha(t, y)$, along $y = 4$ mm.

Figure 5. Comparison between measured void fractions in straight pipe and the Smith [14] correlation.

Figure 6. Void fraction estimated using the Mauro et al. [23] liquid film thickness model. (a) predicted gas-liquid interface in pipe cross section ($J_G = 11.8$ m/s, $J_L = 0.098$ m/s); (b) comparisons between calculated α and data. Dotted lines: $\pm$5% errors; Dashed lines: $\pm$10% errors.

Figure 7. Measured void fractions in straight pipe compared with the drift-flux model with optimized C_0 and V_{Gj} (closed symbols) and the Chexal et al. [13] correlation (open symbols). The dotted lines represent $\pm$10% errors.

Figure 8. Upward flow in bend ($J_G = 3.98$ m/s and $J_L = 0.19$ m/s; slug flow).

Figure 9. Upward flow in bend ($J_G = 0.69$ m/s and $J_L = 0.43$ m/s; plug flow).

Figure 10. Void fraction distribution of downward annular flow obtained by time-strip image analysis. J_G = 7.8 m/s, J_L = 0.092 m/s. (a) straight section; (b) $\theta_B = 3\pi/4$; (c) $\theta_B = \pi/2$; (d) $\theta_B = \pi/4$. The flow direction is from left to right.

Figure 11. Void fraction distribution of upward annular flow obtained by time-strip image analysis. J_G = 7.8 m/s, J_L = 0.090 m/s. (a) straight section; (b) $\theta_B = \pi/4$; (c) $\theta_B = \pi/2$; (d) $\theta_B = 3\pi/4$. The flow direction is from left to right.

Figure 12. Void fraction distribution of downward slug flow obtained by time-strip image analysis. J_G = 1.35 m/s, J_L = 0.50 m/s. (a) straight section; (b) $\theta_B = 3\pi/4$; (c) $\theta_B = \pi/2$; (d) $\theta_B = \pi/4$. The flow direction is the left to the right.

Figure 13. Void fraction distribution of upward slug flow obtained by time-strip image analysis. J_G = 1.35 m/s, J_L = 0.49 m/s. (a) straight section; (b) $\theta_B = \pi/4$; (c) $\theta_B = \pi/2$; (d) $\theta_B = 3\pi/4$. The flow direction is the left to the right.

Figure 14. Comparison between void fractions in straight section, upward flow in bend and downward flow in bend. S: straight section; U: upward flow; D: downward flow.

Figure 15. The ratio, V^*, of the mixture velocity to the liquid velocity. The data are obtained by substituting the measured values of the void fraction, the quality and e = 0.4 into Eq. (3). The solid line is the Smith [14] correlation, Eq. (4).

Figure 16. Measured void fractions in bend in comparison with the Usui et al. [9] correlation. The dotted lines represent $\pm$10% errors, and the dashed lines are for $\pm$20% errors.

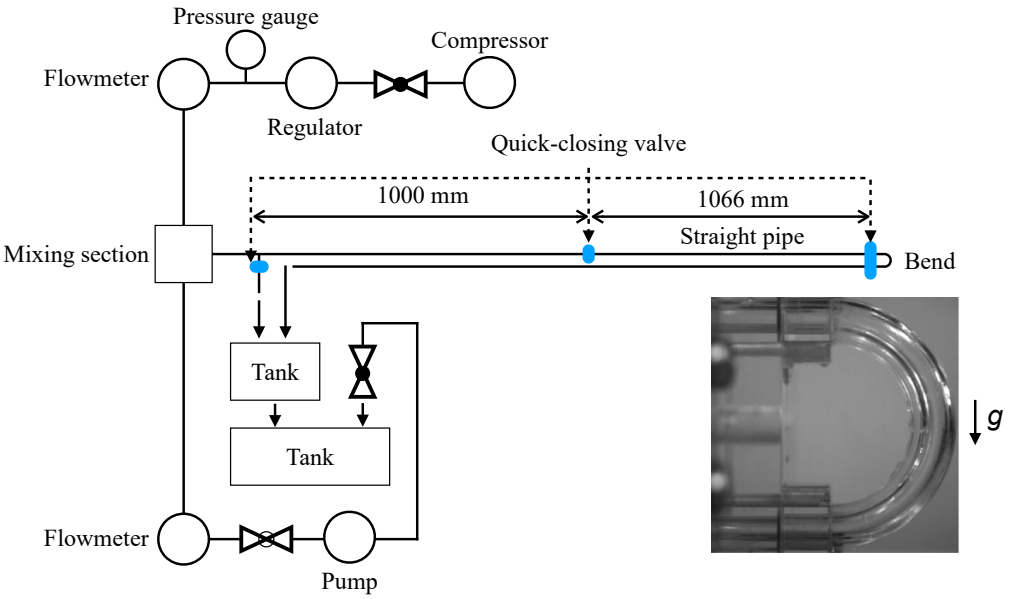

Figure 1. Experimental setup.

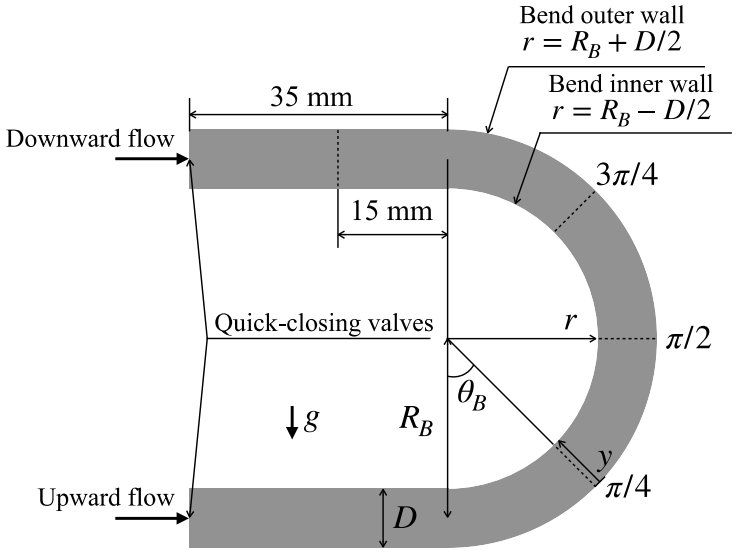

Figure 2. Bend configuration.

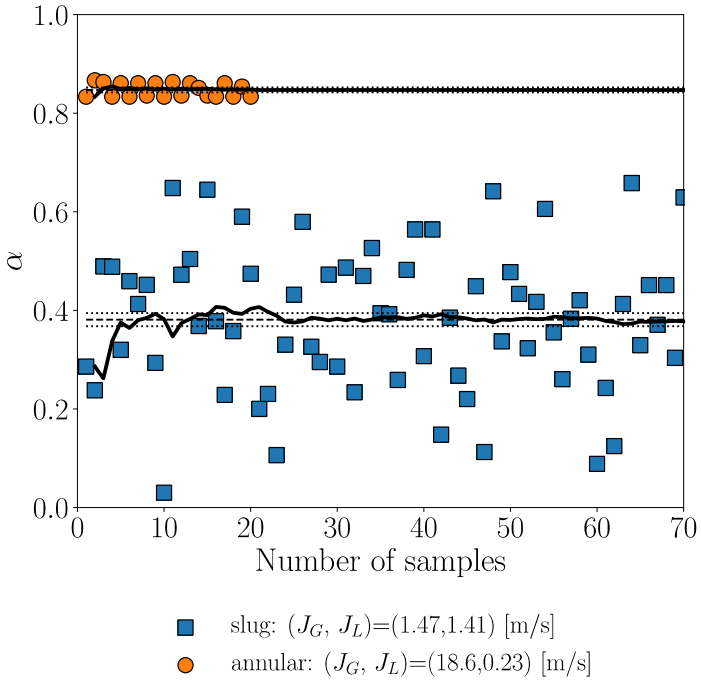

Figure 3. Measured void fractions in bend and their mean values changing with number of samples.

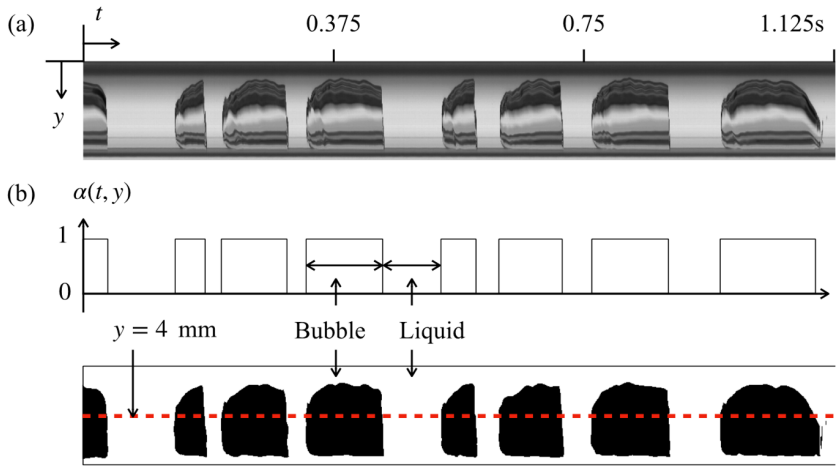

Figure 4. Time-strip image of plug flow. (a) time-strip image at $\theta_B = \pi/4$; (b) binarized time-strip image and waveform of void fraction, $\alpha(t, y)$, along $y = 4$ mm.

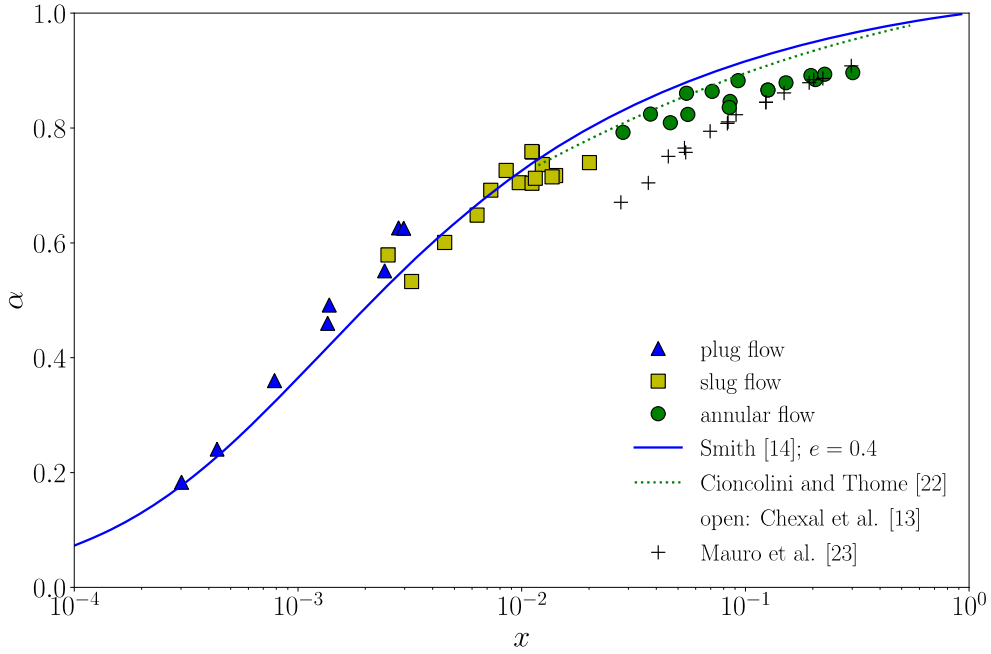

Figure 5. Comparison between measured void fractions in straight pipe and the Smith [14] correlation.

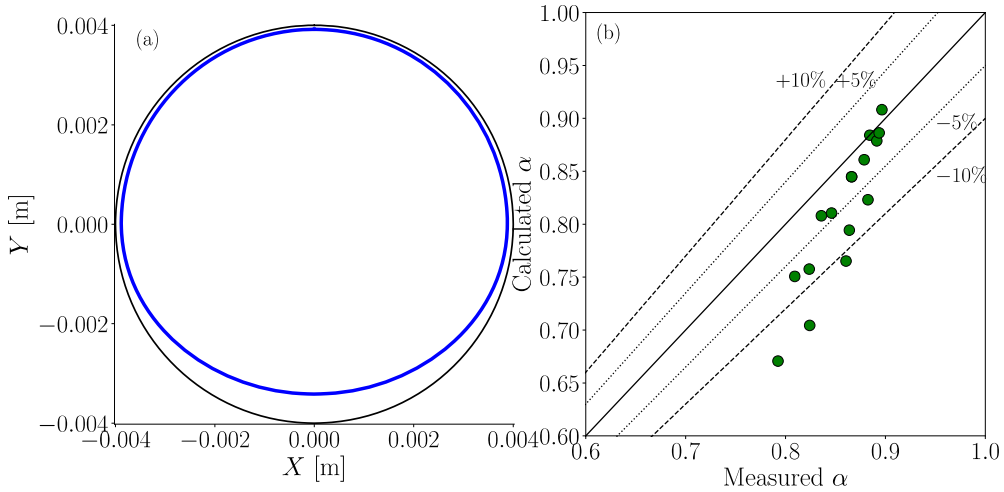

Figure 6. Void fraction estimated using the Mauro et al. [23] liquid film thickness model. (a) predicted gas-liquid interface in pipe cross section (J_G = 11.8 m/s, J_L = 0.098 m/s); (b) comparisons between calculated α and data. Dotted lines: $\pm$5% errors; Dashed lines: $\pm$10% errors.

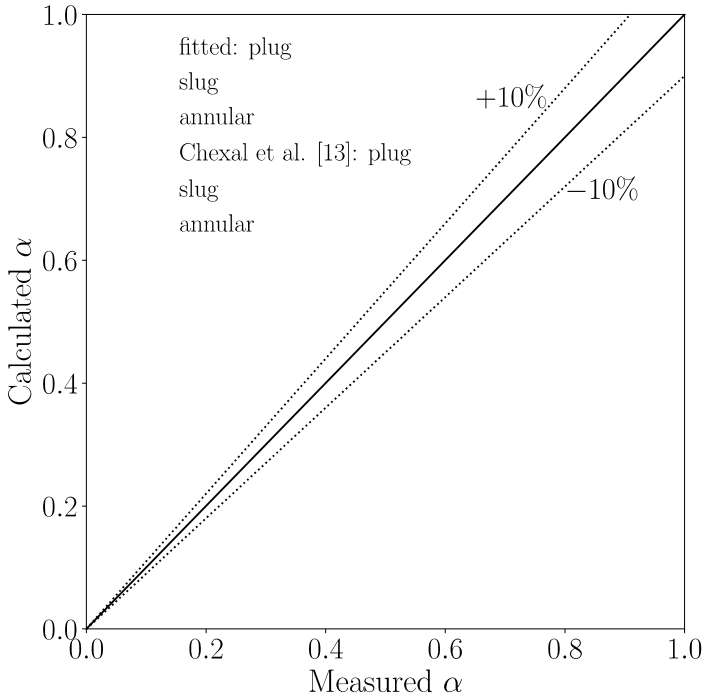

Figure 7. Measured void fractions in straight pipe compared with the drift-flux model with optimized C_0 and V_{Gj} (closed symbols) and the Chexal et al. [13] correlation (open symbols). The dotted lines represent $\pm$10% errors.

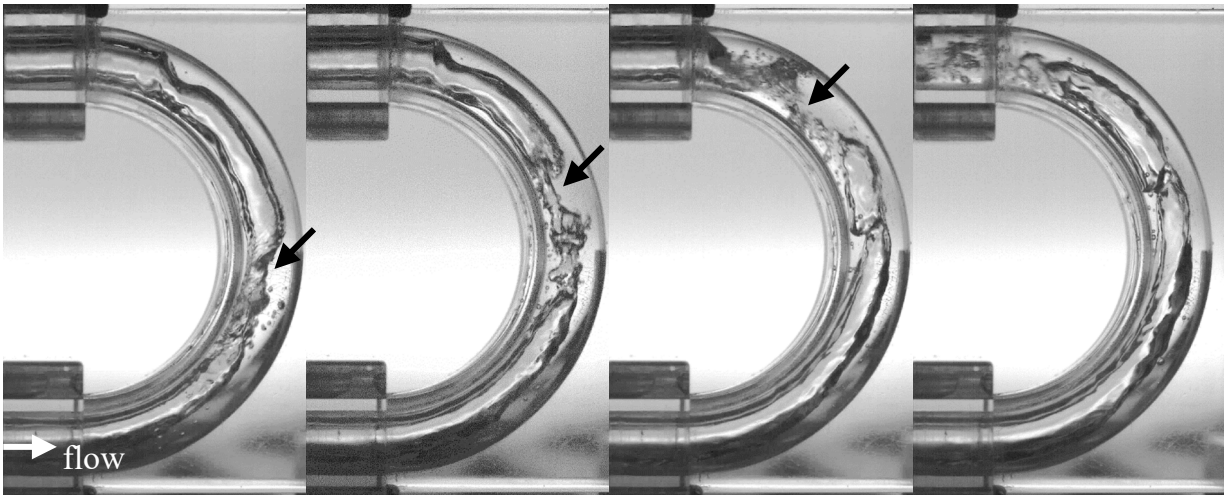

(a) t_1 (b) t_1+5 ms (c) t_1+10 ms (d) t_1+15 ms

Figure 8. Upward flow in bend (J_G = 3.98 m/s and J_L = 0.19 m/s; slug flow).

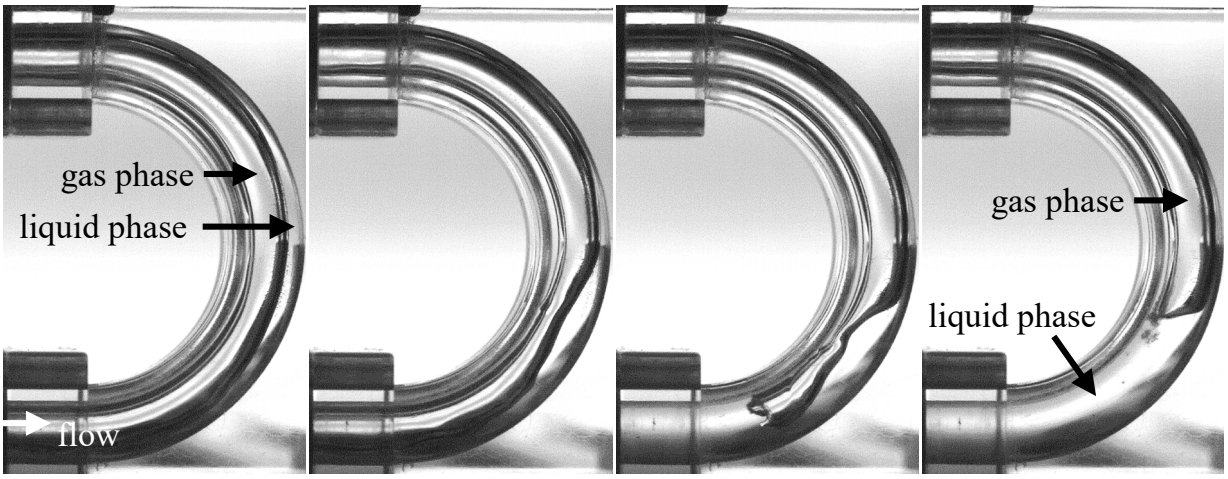

(a) t_1 (b) t_1+43 ms (c) t_1+62 ms (d) t_1+67 ms

Figure 9. Upward flow in bend (J_G = 0.69 m/s and J_L = 0.43 m/s; plug flow).

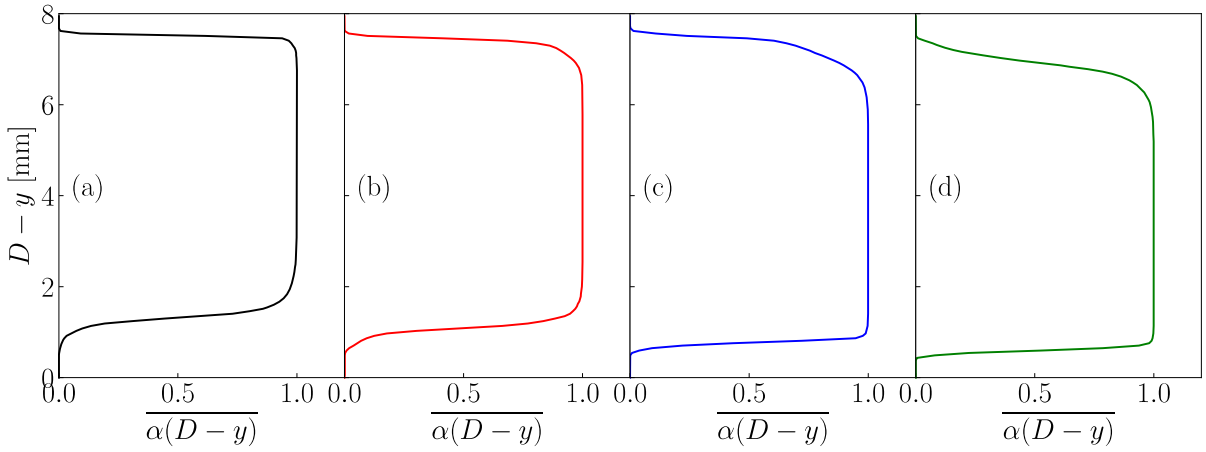

Figure 10. Void fraction distribution of downward annular flow obtained by time-strip image analysis. J_G = 7.8 m/s, J_L = 0.092 m/s. (a) straight section; (b) $\theta_B = 3\pi/4$; (c) $\theta_B = \pi/2$; (d) $\theta_B = \pi/4$. The flow direction is from left to right.

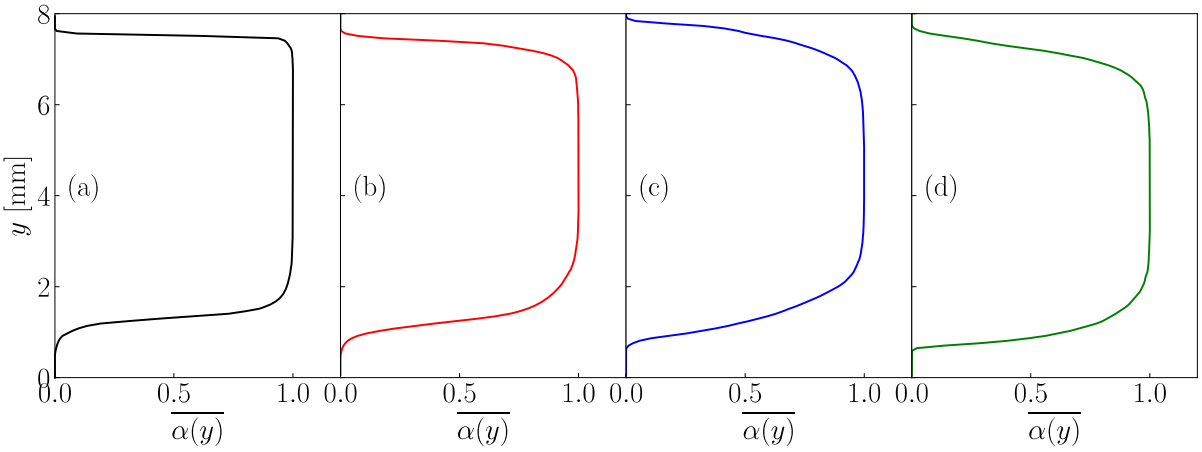

Figure 11. Void fraction distribution of upward annular flow obtained by time-strip image analysis. J_G = 7.8 m/s, J_L = 0.090 m/s. (a) straight section; (b) $\theta_B = \pi/4$; (c) $\theta_B = \pi/2$; (d) $\theta_B = 3\pi/4$. The flow direction is from left to right.

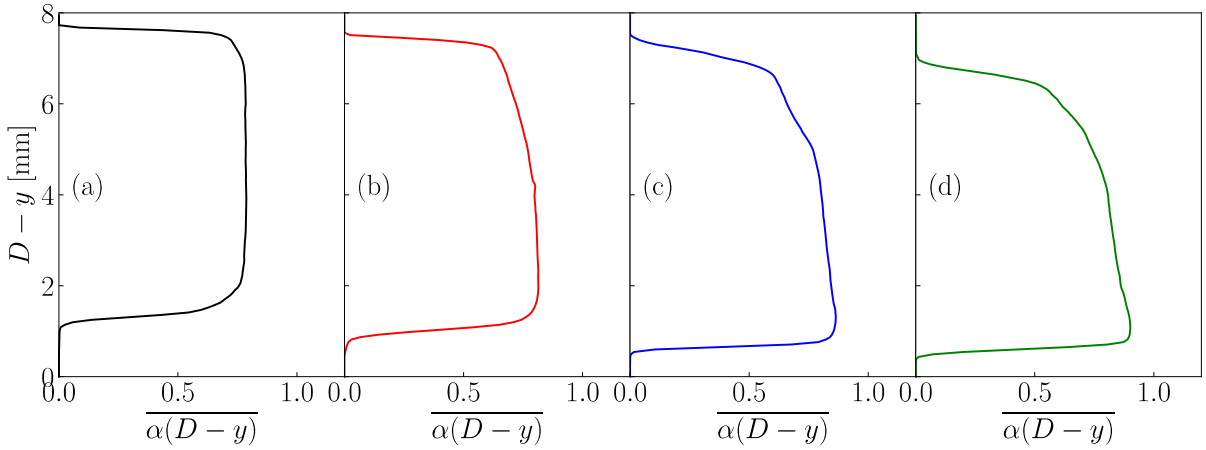

Figure 12. Void fraction distribution of downward slug flow obtained by time-strip image analysis. J_G = 1.35 m/s, J_L = 0.50 m/s. (a) straight section; (b) $\theta_B = 3\pi/4$; (c) $\theta_B = \pi/2$; (d) $\theta_B = \pi/4$. The flow direction is the left to the right.

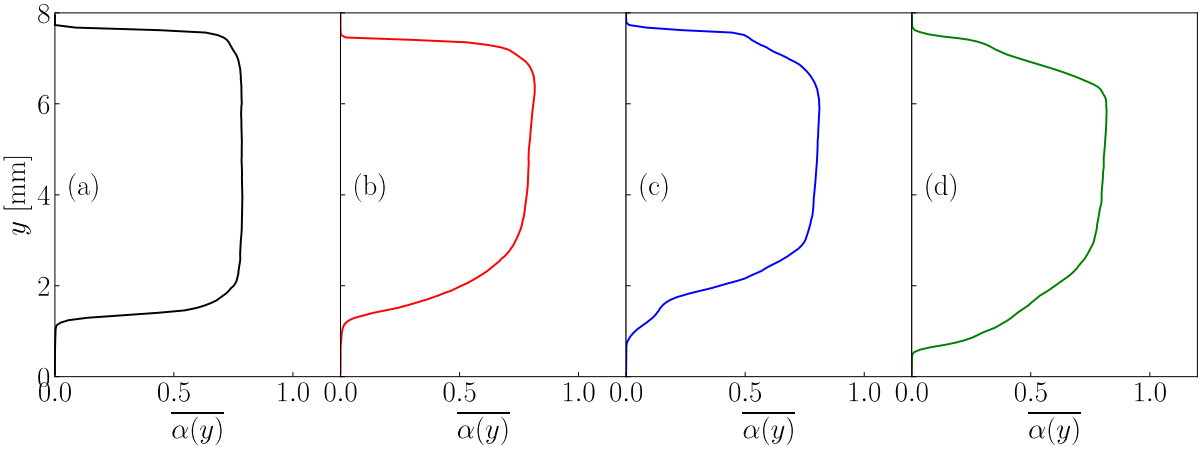

Figure 13. Void fraction distribution of upward slug flow obtained by time-strip image analysis. J_G = 1.35 m/s, J_L = 0.49 m/s. (a) straight section; (b) $\theta_B = \pi/4$; (c) $\theta_B = \pi/2$; (d) $\theta_B = 3\pi/4$. The flow direction is the left to the right.

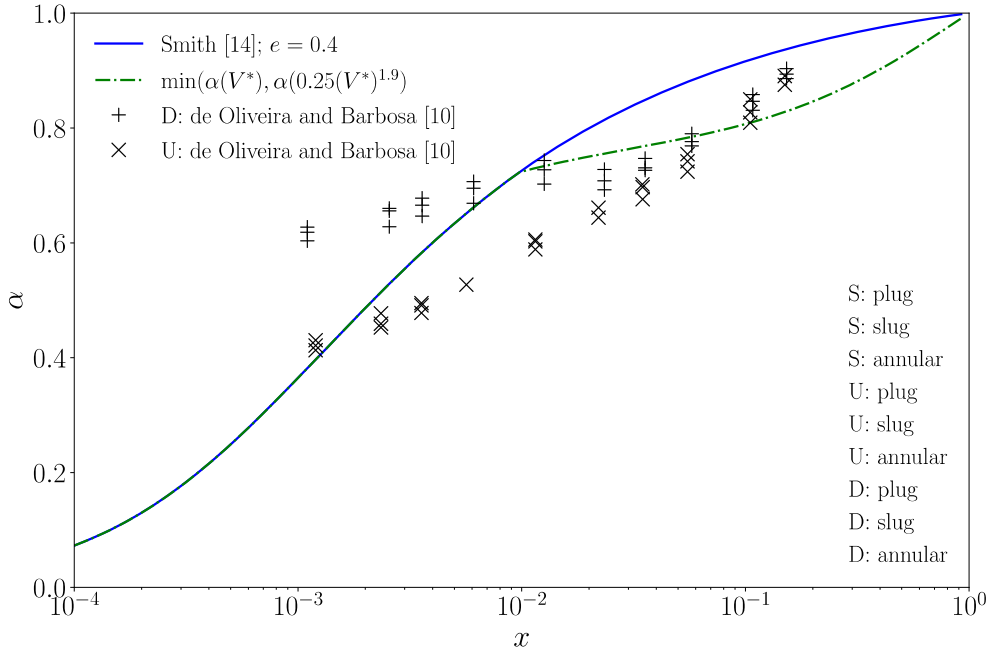

Figure 14. Comparison between void fractions in straight section, upward flow in bend and downward flow in bend. S: straight section; U: upward flow; D: downward flow.

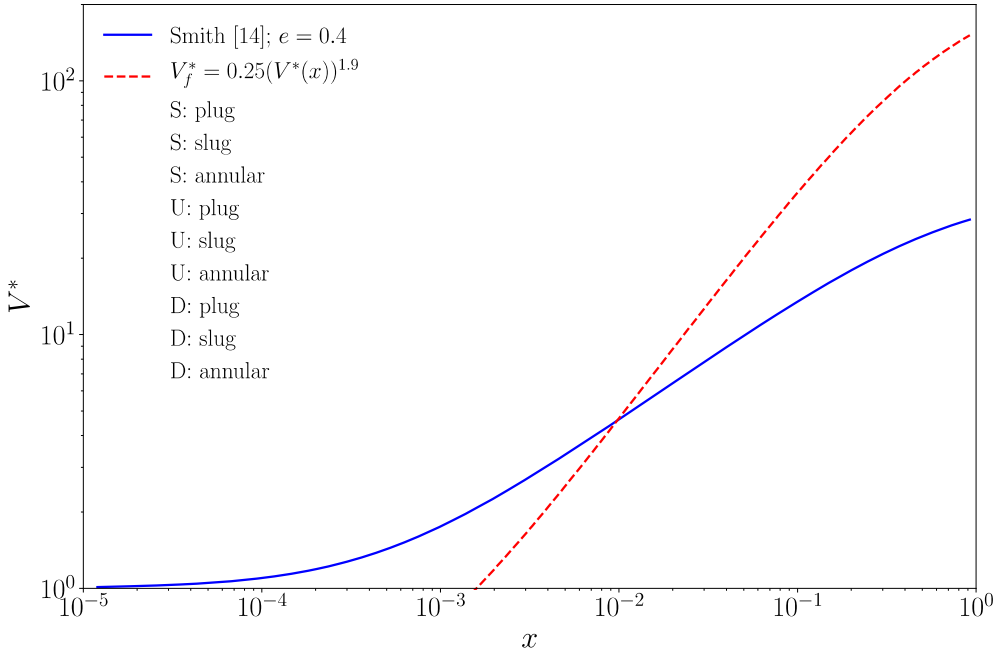

Figure 15. The ratio, V^*, of the mixture velocity to the liquid velocity. The data are obtained by substituting the measured values of the void fraction, the quality and e = 0.4 into Eq. (3). The solid line is the Smith [14] correlation, Eq. (4).

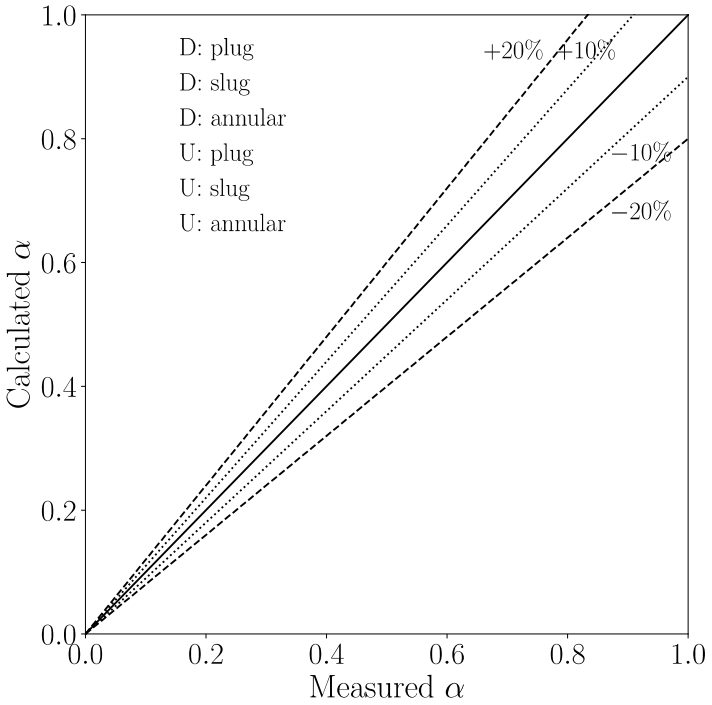

Figure 16. Measured void fractions in bend in comparison with the Usui et al. [9] correlation. The dotted lines represent ±10% errors, and the dashed lines are for ±20% errors.